

# Transition from intrinsic to extrinsic anomalous Hall effect in the ferromagnetic Weyl semimetal $\text{PrAlGe}_{1-x}\text{Si}_x$

Cite as: APL Mater. 8, 011111 (2020); doi: 10.1063/1.5132958

Submitted: 21 October 2019 • Accepted: 3 January 2020 •

Published Online: 16 January 2020



Hung-Yu Yang,<sup>1</sup> Bahadur Singh,<sup>2,3</sup> Baozhu Lu,<sup>4</sup> Cheng-Yi Huang,<sup>5</sup> Faranak Bahrami,<sup>1</sup> Wei-Chi Chiu,<sup>2</sup> David Graf,<sup>6</sup> Shin-Ming Huang,<sup>7</sup> Baokai Wang,<sup>2</sup> Hsin Lin,<sup>5</sup> Darius Torchinsky,<sup>4</sup> Arun Bansil,<sup>2</sup> and Fazel Tafti<sup>1,a)</sup>

## AFFILIATIONS

<sup>1</sup>Department of Physics, Boston College, Chestnut Hill, Massachusetts 02467, USA

<sup>2</sup>Department of Physics, Northeastern University, Boston, Massachusetts 02115, USA

<sup>3</sup>SZU-NUS Collaborative Center and International Collaborative Laboratory of 2D Materials for Optoelectronic Science & Technology, Engineering Technology Research Center for 2D Materials Information Functional Devices and Systems of Guangdong Province, College of Optoelectronic Engineering, Shenzhen University, Shenzhen 518060, China

<sup>4</sup>Department of Physics and Temple Materials Institute, Temple University, Philadelphia, Pennsylvania 19122, USA

<sup>5</sup>Institute of Physics, Academia Sinica, Taipei 11529, Taiwan

<sup>6</sup>National High Magnetic Field Laboratory, Tallahassee, Florida 32310, USA

<sup>7</sup>Department of Physics, National Sun Yat-sen University, Kaohsiung 80424, Taiwan

**Note:** This paper is part of the Special Topic on Topological Semimetals—New Directions.

<sup>a)</sup>**Author to whom correspondence should be addressed:** fazel.tafti@bc.edu

## ABSTRACT

Recent reports of a large anomalous Hall effect (AHE) in ferromagnetic Weyl semimetals (FM WSMs) have led to a resurgence of interest in this enigmatic phenomenon. However, due to a lack of tunable materials, the interplay between the intrinsic mechanism caused by Berry curvature and extrinsic mechanisms due to scattering remains unclear in FM WSMs. In this contribution, we present a thorough investigation of both the extrinsic and intrinsic AHEs in a new family of FM WSMs,  $\text{PrAlGe}_{1-x}\text{Si}_x$ , where  $x$  can be tuned continuously. Based on the first-principles calculations, we show that the two end members,  $\text{PrAlGe}$  and  $\text{PrAlSi}$ , have different Fermi surfaces, but similar Weyl node structures. Experimentally, we observe moderate changes in the anomalous Hall coefficient ( $R_S$ ), but significant changes in the ordinary Hall coefficient ( $R_0$ ) in  $\text{PrAlGe}_{1-x}\text{Si}_x$  as a function of  $x$ . By comparing the magnitude of  $R_0$  and  $R_S$ , we identify two regimes:  $|R_0| < |R_S|$  for  $x \leq 0.5$  and  $|R_0| > |R_S|$  for  $x > 0.5$ . Through a detailed scaling analysis, we uncover a universal anomalous Hall conductivity (AHC) from intrinsic contribution when  $x \leq 0.5$ . Such a universal AHC is absent for  $x > 0.5$ . Our study, thus, reveals the significance of extrinsic mechanisms in FM WSMs and reports the first observation of the transition from the intrinsic to extrinsic AHE in  $\text{PrAlGe}_{1-x}\text{Si}_x$ .

© 2020 Author(s). All article content, except where otherwise noted, is licensed under a Creative Commons Attribution (CC BY) license (<http://creativecommons.org/licenses/by/4.0/>). <https://doi.org/10.1063/1.5132958>

## I. INTRODUCTION

The Hall effect in ferromagnets is commonly characterized by the following empirical formula for the Hall resistivity  $\rho_{xy}$ :<sup>1,2</sup>

$$\rho_{xy} = \rho_{xy}^O + \rho_{xy}^A = R_0 H_z + R_S M_z, \quad (1)$$

where  $R_0$  and  $R_S$  are ordinary and anomalous Hall coefficients, respectively. The ordinary Hall effect ( $\rho_{xy}^O$ ) is linearly proportional to the applied magnetic field ( $H_z$ ) through  $R_0$ , which is simply related to a carrier concentration in a single-band metal. The anomalous Hall effect (AHE)  $\rho_{xy}^A$ , however, is proportional to the ferromagnetic moment  $M_z$  through  $R_S$ , which involves a complicated

combination of extrinsic and intrinsic mechanisms. The main extrinsic mechanisms are skew-scattering<sup>3</sup> and side-jump,<sup>4</sup> both of which are related to the scattering between electrons and impurities with spin-orbit coupling. In contrast, the intrinsic (Karplus-Luttinger) mechanism originates from an anomalous velocity resulting from a phase shift in the electronic wave-packet, which is independent of impurities.<sup>5,6</sup> Since the reformulation of the intrinsic mechanism in terms of Berry curvature,<sup>6,7</sup> this concept has been invoked to explain the AHE in the canonical AHE material, bcc iron.<sup>8</sup> The intrinsic mechanism is gaining increasing attention because it is also applicable to the AHE in Weyl semimetals (WSMs) where the Weyl nodes, monopoles of the Berry curvature, can potentially generate a large AHE.<sup>9</sup> Recently, several WSMs have been found to exhibit such a large AHE, including pyrochlore iridates (Nd<sub>2</sub>Ir<sub>2</sub>O<sub>7</sub>),<sup>10,11</sup> Heusler and half-Heusler compounds (Co<sub>2</sub>MnGa and GdPtBi),<sup>12–14</sup> and ferromagnetic (FM) WSMs, such as shandite structures (Co<sub>3</sub>Sn<sub>2</sub>S<sub>2</sub>).<sup>15</sup> All these discoveries have been interpreted as an intrinsic AHE, and the extrinsic contributions have been overlooked. For example, in the topological ferromagnet Fe<sub>3</sub>Sn<sub>2</sub>, the intrinsic contribution to the AHE is confirmed via a scaling analysis, but the extrinsic contribution could be five times larger than the intrinsic one.<sup>16,17</sup> In addition, most studies of the AHE are based on the analysis of a single compound and are, therefore, quite limited in their ability to distinguish between extrinsic and intrinsic contributions. One experimental approach to address this issue would be to maintain the structure of the Weyl nodes but change the Fermi surface (or vice versa) across a series of compositions and tune the relative magnitude of extrinsic and intrinsic AHE contributions. This is precisely the subject of the present article where we explored this possibility in the FM WSMs PrAlGe<sub>1-x</sub>Si<sub>x</sub>. We study the AHE in PrAlGe<sub>1-x</sub>Si<sub>x</sub> alloys with  $x = 0, 0.25, 0.5, 0.7, 0.85,$  and  $1$  to investigate both intrinsic and extrinsic contributions to the AHE in this tunable FM WSM family. Although the end members, PrAlGe and PrAlSi, are both FM WSMs with the same number of Weyl nodes, we reveal a transition of the AHE from an intrinsic ( $x \leq 0.5$ ) to an extrinsic regime ( $x > 0.5$ ). The significance of our results is twofold. First, we demonstrate the importance of extrinsic contributions to the AHE even in a FM WSM with robust Weyl nodes. Second, we reveal a transition from intrinsic to extrinsic AHEs in the same family of FM WSMs and show the possibility of tuning AHE in topological semimetals.

## II. EXPERIMENTAL METHODS

### A. Crystal growth

Single crystals of PrAlGe<sub>1-x</sub>Si<sub>x</sub> were grown using a self-flux method from Pr ingots (99.00%, Alfa Aesar), Al lumps (99.5%, Alfa Aesar), Ge pieces (99.999%+, Alfa Aesar), and Si lumps (99.999%+, Alfa Aesar). The starting chemicals were mixed with the mole ratio Pr:Al:Ge:Si = 1:10:1 -  $y:y$ , placed in a crucible inside an evacuated quartz tube, heated to 1000 °C at 180 °C/h, stayed at 1000 °C for 12 h, cooled to 700 °C at 6 °C/h, and annealed at 700 °C for another 12 h. Then, the tube was centrifuged to remove the excess Al flux. All crystals of PrAlGe<sub>1-x</sub>Si<sub>x</sub> were plate-like with the surface of the plate normal to the  $c$ -axis and its edges along the  $a$ -axis. The chemical composition of each crystal was determined by energy dispersive x-ray spectroscopy (EDX) using a ZEISS Ultra-55 field emission

scanning electron microscope equipped with an EDAX detector. Our EDX analysis (Appendix A) showed that  $x = y$  in PrAlGe<sub>1-x</sub>Si<sub>x</sub> samples with  $y = 0, 0.5,$  and  $1$ . However, samples with  $y = 0.75$  and  $0.9$  turned out to have  $x = 0.7$  and  $0.85,$  respectively, as given in Table I of Appendix A.

Notably, single crystals of PrAlGe made by flux growth and floating zone technique that have been reported in the literature show slightly different properties.<sup>18,19</sup> The resistivity and magnetization characteristics of our PrAlGe samples are similar to those reported in Ref. 18 with a residual resistivity ratio (RRR)  $\approx 2.2,$  which is 70% larger than that of the samples grown by a floating zone technique (RRR  $\approx 1.3$  in Ref. 19). Unlike the samples in Ref. 19, the EDX results in Appendix A also show that our samples are not Al-rich as we used a smaller quantity of Al-flux. We performed EDX measurements on three samples from each batch. The standard error for each composition is less than 1%, even though EDX can have accuracy errors of up to 5%. The EDX detector was calibrated with both Al and Si standards prior to the measurements.

### B. Measurements

Electrical resistivity was measured with a standard four-probe technique, and the heat capacity was measured with a relaxation time method in a Quantum Design physical property measurement system (PPMS) Dynacool. The dc magnetization experiment was conducted on the vibrating sample magnetometer in a Quantum Design MPMS3. The high-field experiment was performed in a 35 T dc Bitter magnet inside a <sup>3</sup>He fridge at a base temperature of 300 mK at the National High Magnetic Field laboratory in Tallahassee. All samples used for transport measurements were carefully sanded to remove the residual Al-flux and to have the ideal bar geometry for the determination of resistivity.

### C. Calculations

Electronic structure calculations were performed within the framework of the density functional theory (DFT) using the experimental lattice parameters and the projector augmented wave (PAW) method implemented in the Vienna *ab initio* simulation package (VASP).<sup>20</sup> Exchange-correlation effects were included using the generalized gradient approximation (GGA), and the spin-orbit coupling effects were included self-consistently.<sup>21,22</sup> An on-site Coulomb interaction was added for Pr  $f$ -electrons within the GGA + U scheme with  $U_{\text{eff}} = 6$  eV. An effective Wannier tight-binding Hamiltonian was obtained from the *ab initio* results by using the VASP2WANNIER90 interface. This Hamiltonian was subsequently used to obtain topological properties.<sup>23</sup>

### D. Second harmonic generation

The second-harmonic-generation (SHG) data were taken at normal incidence from the [101] face of the as-grown crystals for incoming (outgoing) wavelengths 1500 (750) nm as a function of the incoming field polarization and measured for emitted light polarized parallel to the [010] crystalline axis. In this geometry, all bulk contributions to SHG from a  $I4_1/amd$  space group are forbidden, including the bulk magnetic dipolar, electric quadrupolar, and electric-field induced SHG.

### III. RESULTS

#### A. Crystal structure

PrAlGe and PrAlSi are both WSMs due to broken inversion symmetry<sup>24</sup> similar to the archetypal WSM, TaAs.<sup>25,26</sup> However, they undergo an FM transition at  $T_C = 15\text{--}17$  K, unlike TaAs which remains non-magnetic at all temperatures. As shown in Figs. 1(a) and 1(b), TaAs and the PrAlGe<sub>1-x</sub>Si<sub>x</sub> crystallize in the same noncentrosymmetric space group ( $I4_1md$ ) with the important difference that the Pr atoms in PrAlGe<sub>1-x</sub>Si<sub>x</sub> provide a net magnetic moment along the  $c$ -axis below  $T_C$ . Furthermore, a solid solution of Ge and Si is realized in PrAlGe<sub>1-x</sub>Si<sub>x</sub>, which results in a continuous change of lattice parameters, as shown in Fig. 1(c). The lattice parameters in Fig. 1(c) are obtained from the Rietveld refinement of the powder x-ray diffraction data in the non-centrosymmetric space group  $I4_1md$  (Appendix B). The point group  $C_{4v}$  is confirmed by SHG refinements in Appendix C. This structure is characteristic of the entire RAlSi(Ge) family ( $R$  = rare-earth) and generally leads to the appearance of Weyl nodes in their band structure,<sup>24</sup> as observed in LaAlGe,<sup>27</sup> CeAlGe,<sup>28</sup> PrAlGe,<sup>18</sup> and CeAlSi<sub>0.3</sub>Ge<sub>0.7</sub>.<sup>29</sup> As we will see, the number and

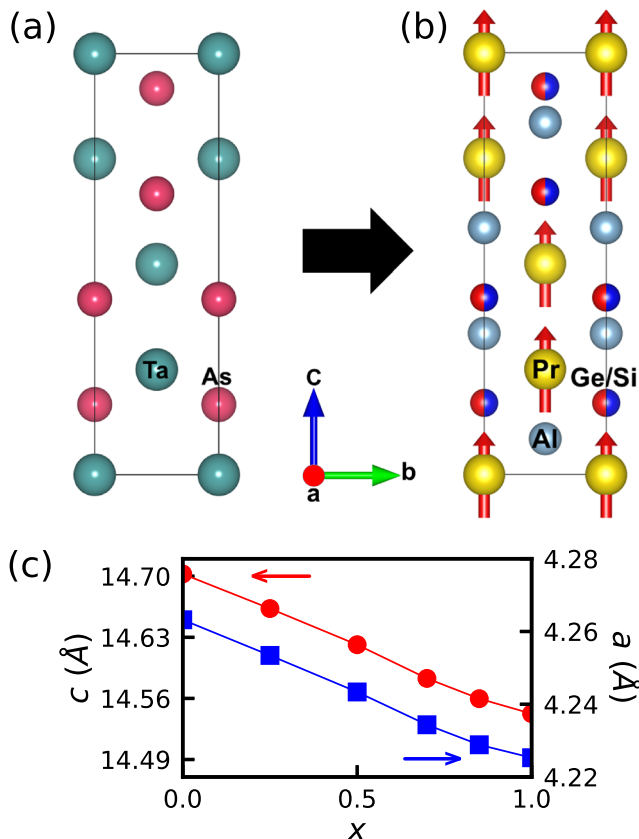


**FIG. 1.** (a) Crystal structure of TaAs in the space group  $I4_1md$  (No. 109). (b) The unit cell of PrAlGe<sub>1-x</sub>Si<sub>x</sub>, which is similar to that of TaAs, but with additional Al atoms. (c) Continuous change of lattice parameters as a function of  $x$  among PrAlGe<sub>1-x</sub>Si<sub>x</sub> compounds.

positions of the Weyl nodes are similar in PrAlGe<sub>1-x</sub>Si<sub>x</sub> at different  $x$ , but the Fermi surface significantly changes across the series, giving rise to two regimes of the AHE in the PrAlGe<sub>1-x</sub>Si<sub>x</sub> family.

#### B. Magnetic properties

A combination of magnetization and heat capacity measurements reveals the FM order, hence the breaking of time-reversal symmetry. The magnetic properties are similar among PrAlGe<sub>1-x</sub>Si<sub>x</sub> samples, as Fig. 2 shows representative data at  $x = 0, 0.5$ , and 1. The magnetic susceptibility is two orders of magnitude larger when measured with  $H \parallel c$  [ $\chi_c$  in Fig. 2(a)] compared to  $H \parallel a$  [ $\chi_a$  in Fig. 2(b)], indicating a strong Ising-like magnetic anisotropy. Based on a Curie-Weiss analysis (see Appendix D), the three samples have comparable Weiss temperatures  $\Theta_W = 30\text{--}40$  K and effective moments  $\mu_{\text{eff}} = 3.4\text{--}3.7 \mu_B$ , as expected from Pr<sup>3+</sup> ( $3.56 \mu_B$ ). The FM transition temperature  $T_C$  is evaluated from the peak in the heat capacity data, which yields  $T_C = 15.1(2), 16.3(2)$ , and  $17.2(2)$  for PrAlGe, PrAlGe<sub>0.5</sub>Si<sub>0.5</sub>, and PrAlSi, respectively [see Fig. 2(c)]. The magnetization curves with  $H \parallel c$  and  $H \parallel a$  are compared in Fig. 2(d), where  $M(H \parallel c)$  saturates at approximately 0.5 T, but  $M(H \parallel a)$  does not. This is consistent with  $\chi_c \gg \chi_a$  in Fig. 2(a) and the Ising anisotropy depicted in Fig. 1(b) with the  $c$ -axis as the magnetic easy-axis. The saturated moment for all PrAlGe<sub>1-x</sub>Si<sub>x</sub> samples is approximately  $3.3 \mu_B/\text{Pr}$ .

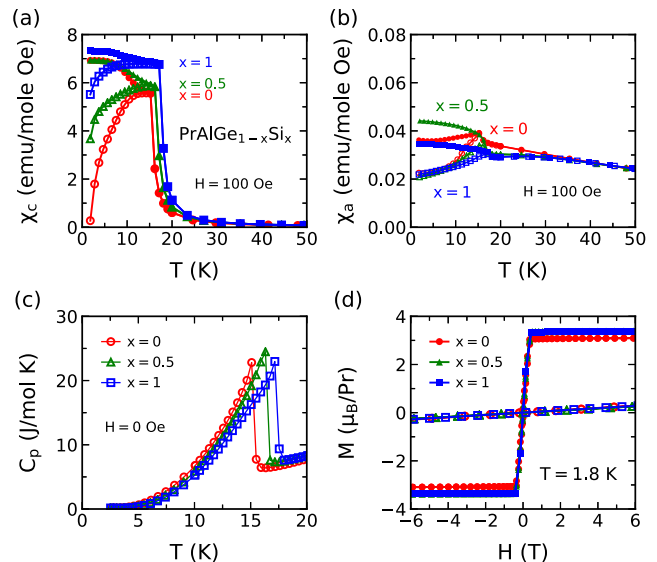


**FIG. 2.** (a) Magnetic susceptibility measured as a function of temperature with field parallel to the  $c$ -axis ( $\chi_c$ ). Red circles, green triangles, and blue squares represent the data for PrAlGe, PrAlGe<sub>0.5</sub>Si<sub>0.5</sub>, and PrAlSi, respectively (in all four panels). Empty and full symbols correspond to zero-field-cooling (ZFC) and field-cooling (FC), respectively. (b) Susceptibility data with field parallel to the  $a$ -axis ( $\chi_a$ ). Note that the  $y$ -scale is 100 times smaller than in panel (a) due to the Ising-like magnetic anisotropy. (c) Heat capacity as a function of temperature. The peaks correspond to  $T_C$ . (d) Magnetization as a function of field parallel to  $c$ - and  $a$ -axes (full and open symbols). Note that the coercive field is less than 0.1 T, and so the hysteresis loop is not visible on this scale.

In summary, the magnetic properties of  $\text{PrAlGe}_{1-x}\text{Si}_x$  samples are nearly identical.

### C. Band structure

We incorporated the crystalline and magnetic structures of  $\text{PrAlGe}$  and  $\text{PrAlSi}$  in our DFT calculations to arrive at realistic band structures. Even in a non-magnetic calculation, these compounds are Weyl semimetals due to broken inversion symmetry, similar to  $\text{LaAlGe}$ .<sup>27</sup> Including magnetism in DFT calculations shifts the location of Weyl nodes in  $k$ -space without changing their number. We compare the calculated band structures, Fermi surfaces, and Weyl nodes in  $\text{PrAlGe}$  [Figs. 3(a), 3(c), and 3(e)] and  $\text{PrAlSi}$  [Figs. 3(b), 3(d), and 3(f)]. The band structure of both systems in Figs. 3(a) and 3(b) include tilted crossings near  $\Sigma$  and  $\Sigma_1$  characteristic of type-II Weyl semimetals. The hole pocket between  $\Sigma_1$

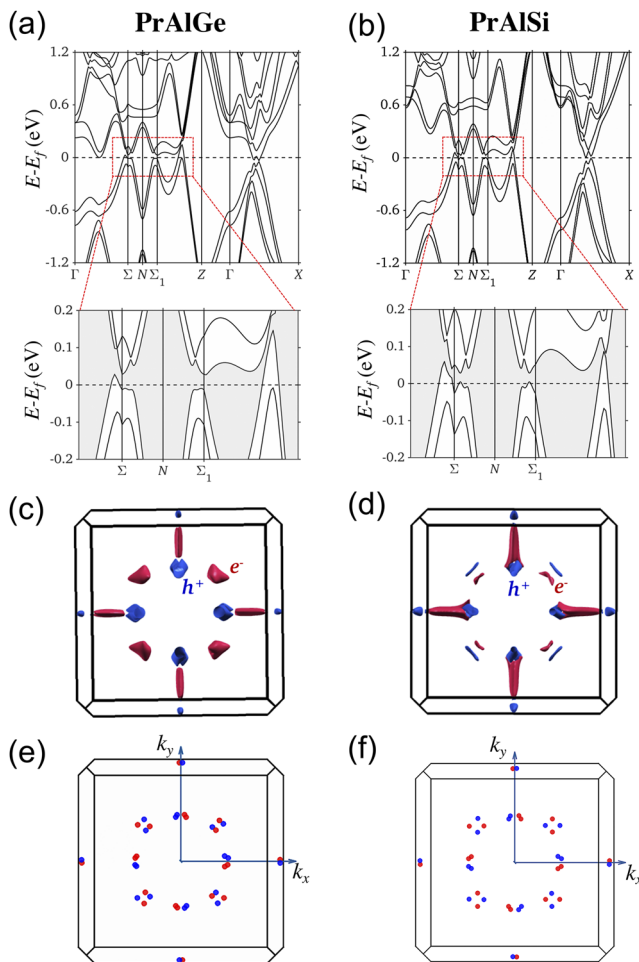


**FIG. 3.** A comparison is made between the band structures [(a) and (b)], Fermi surfaces [(c) and (d)], and Weyl nodes [(e) and (f)] in  $\text{PrAlGe}$  and  $\text{PrAlSi}$ , respectively. Both noncentrosymmetric space group symmetry and FM order are considered in the calculations shown here. The shaded region in the closeup band structure shows that valence and conduction bands are well separated along high-symmetry directions.

and  $Z$  is visibly larger in  $\text{PrAlGe}$  than that in  $\text{PrAlSi}$ . The Fermi surface is visualized for both  $\text{PrAlGe}$  and  $\text{PrAlSi}$  in Figs. 3(c) and 3(d) to highlight the larger size and the more isotropic shape of the hole pockets in  $\text{PrAlGe}$  compared to  $\text{PrAlSi}$ . Although the Fermi surfaces are quite different between the two compounds, their Weyl node structures as shown in Figs. 3(e) and 3(f) are quite similar. Both compounds have 40 Weyl nodes located at similar locations in the Brillouin zone. For completeness, we present the nodal structure of  $\text{PrAlGe}_{0.5}\text{Si}_{0.5}$  in Appendix E to confirm the same number of nodes across the entire series of  $\text{PrAlGe}_{1-x}\text{Si}_x$ . Notably, the preservation of topological properties with the substitution of elements is not always guaranteed,<sup>30</sup> and such a preservation in the  $\text{PrAlGe}_{1-x}\text{Si}_x$  family makes it a great platform to study the competition between intrinsic and extrinsic mechanisms of the AHE.

### D. Electronic properties

We observe considerable changes in the magnetoresistance ( $\text{MR}(\%) = 100 \times \frac{\rho_{xx}(H) - \rho_{xx}(0)}{\rho_{xx}(0)}$ ) within the  $\text{PrAlGe}_{1-x}\text{Si}_x$  series. Figures 4(a) and 4(f) show very different temperature dependences of MR between the end members,  $\text{PrAlGe}$  and  $\text{PrAlSi}$ . The

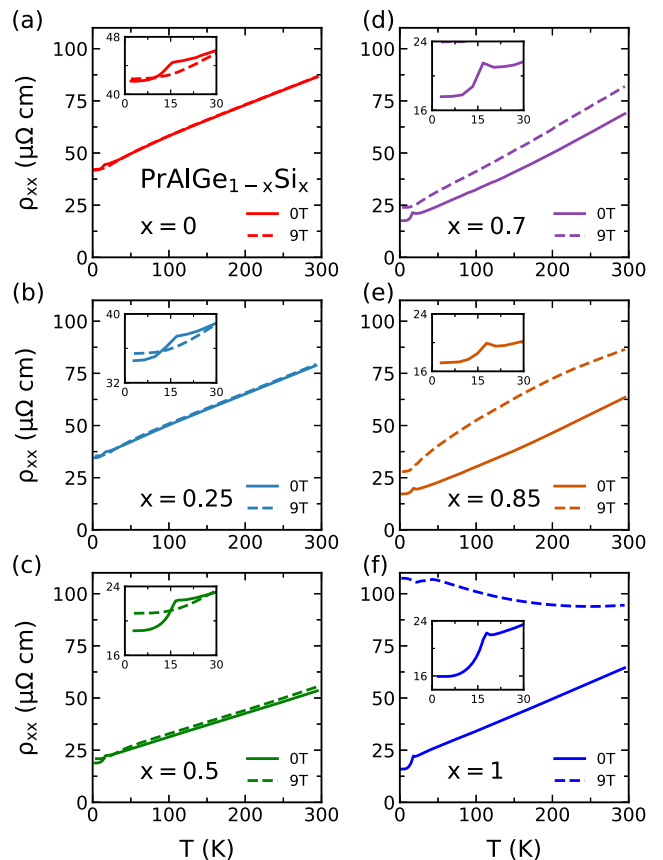


**FIG. 4.** Longitudinal resistivity  $\rho_{xx}$  plotted as a function of  $T$  in each  $\text{PrAlGe}_{1-x}\text{Si}_x$  sample at both  $H = 0$  T and 9 T. The measurement was done with  $I \parallel a$  and  $H \parallel c$ . The Si content for each sample ( $x$ ) is quoted in the corresponding panels [(a)–(f)].

longitudinal resistivity  $\rho_{xx}$  is measured for each sample at both  $H = 0$  (solid line) and 9 T (dashed line). PrAlGe shows a nearly field-independent  $\rho_{xx}$  at  $T > T_C$ , thus, a negligible MR. A weak negative MR is observed near  $T_C$ , which is due to the magnetic fluctuations. In contrast, PrAlSi shows a considerably larger  $\rho_{xx}$  at  $H = 9$  T compared to the zero-field data, thus a strong MR at all temperatures from 1.8 K to 300 K. A continuous evolution of the MR is observed between these two limits in the rest of the PrAlGe $_{1-x}$ Si $_x$  samples in Figs. 4(b)–4(e). The large difference in MR between PrAlGe and PrAlSi can be explained by a different  $\omega_c\tau = H\sigma_{xx}(0)/ne$ , where  $\omega_c$  is the cyclotron frequency,  $\tau$  is the relaxation time,  $\sigma_{xx}(0)$  is the conductivity at 0 T,  $n$  is the carrier concentration, and  $e$  is the electron charge. A rough estimate of  $\omega_c\tau$  at 2 K with data in Figs. 4 and 6 shows that its value in PrAlSi is 20 times larger than in PrAlGe. Therefore, PrAlSi is far more susceptible to the disruptive Lorentz force compared to PrAlGe leading to a much larger MR.

We present field dependences of both MR and Hall effect ( $\rho_{xy}$ ) in Fig. 5. A weak MR is observed in PrAlGe as a function of field at  $T = 30$  K (above  $T_C$ ) in Fig. 5(a) consistent with Fig. 4(a). The MR gradually increases with increasing  $x$  in the PrAlGe $_{1-x}$ Si $_x$  series. Eventually, the MR in PrAlSi ( $x = 1$ ) becomes 100 times larger than the MR in PrAlGe ( $x = 0$ ). This behavior is more pronounced at  $T = 1.8$  K (below  $T_C$ ) in Fig. 5(b). We zoom in the low-field MR data in Fig. 5(c) to show the negative MR due to magnetic fluctuations in all samples. Although the negative MR is more pronounced in samples with higher  $x$  at  $T = 1.8$  K, it never exceeds 4% and disappears at  $T > 2T_C$ , as shown in Fig. 4.

Figure 5(d) shows a variation of the Hall resistivity  $\rho_{xy}(H)$  between different samples at  $T = 30$  K (above  $T_C$ ). The slope of the Hall resistivity  $d\rho_{xy}/dH$  is small and positive at  $H > 1$  T in PrAlGe; it gradually increases with increasing  $x$  and becomes significantly larger in PrAlGe $_{0.15}$ Si $_{0.85}$ . Eventually, it shows an abrupt downturn in PrAlSi (at  $H > 1$  T). This behavior is consistent with our DFT calculations that show smaller hole pockets with increasing Si-content  $x$  in Fig. 3. A gradual weakening of the antibonding orbital overlaps between the  $p$ -orbitals of Al and Ge/Si with increasing  $x$  in PrAlGe $_{1-x}$ Si $_x$  leads to smaller hole and larger electron Fermi surfaces. The  $\rho_{xy}$  behavior at high fields remains unchanged at  $T = 1.8$  K (below  $T_C$ ) as shown in Fig. 5(e). A zoomed-in view at low-fields in Fig. 5(f) reveals the AHE in all samples at  $T = 1.8$  K characterized by a rapid increase in  $\rho_{xy}(H)$  until  $H = 0.5$  T followed by a linear field dependence from  $H = 0.5$  T to 1 T. In Sec. III E, we examine the AHE in detail and reveal a transition from the intrinsic to extrinsic AHE in PrAlGe $_{1-x}$ Si $_x$ .

### E. Anomalous Hall effect

We present two separate analyses to investigate the AHE. The first analysis is based on Eq. (1) to differentiate the relative magnitudes of the ordinary and anomalous Hall coefficients ( $R_0$  and  $R_S$ ) in PrAlGe $_{1-x}$ Si $_x$ . The details of extracting  $R_0$  and  $R_S$  are presented in Appendix F. We plot both  $R_0$  and  $R_S$  as a function of  $x$  in Fig. 6(a) to reveal a crossing between the magnitudes of  $R_0$  and  $R_S$  at  $x = 0.5$  so that  $|R_0|/|R_S| < 1$  at  $x \leq 0.5$ , but  $|R_0|/|R_S| > 1$  at  $x > 0.5$ . The magnitude of  $R_S$  moderately decreases with increasing  $x$  at  $x \leq 0.5$  and remains nearly unchanged afterwards. Whereas  $R_S$  shows only mild variations,  $R_0$  shows considerable variations with  $x$  due

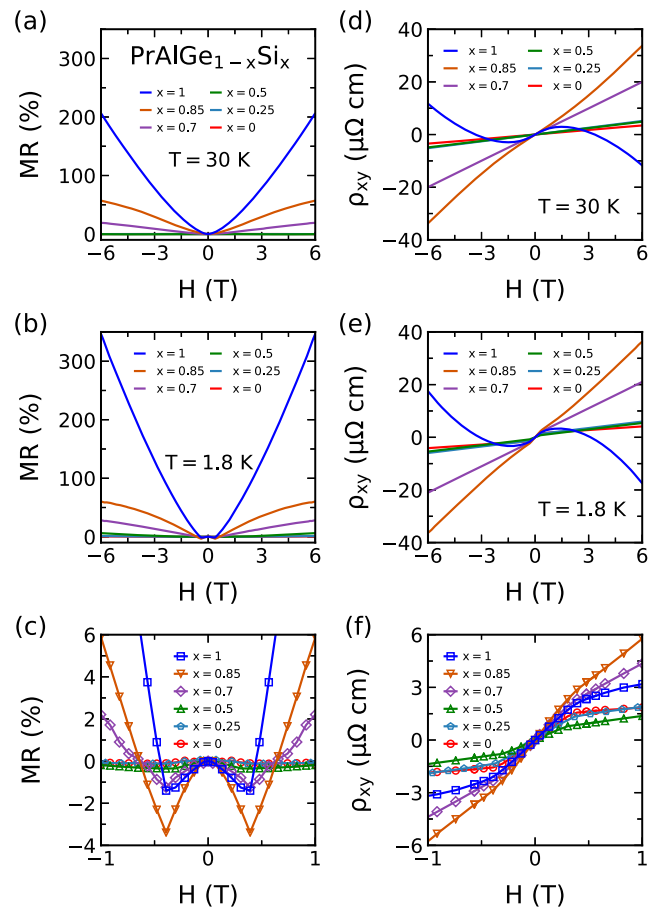


**FIG. 5.** (a) Transverse magnetoresistance in the PrAlGe $_{1-x}$ Si $_x$  samples  $\{MR(\%) = 100 \times [\rho_{xx}(H) - \rho_{xx}(0)]/\rho_{xx}(0)\}$  measured as a function of field at  $T = 30$  K ( $>T_C$ ). The current is along the  $a$ -axis, and the applied field is along the  $c$ -axis ( $z$ ) in all panels. (b) MR at  $T = 1.8$  K ( $<T_C$ ). (c) A zoomed-in view of panel (b) below 1 T. (d) Hall resistivity ( $\rho_{xy}$ ) measured as a function of field at  $T = 30$  K ( $>T_C$ ). (e)  $\rho_{xy}$  at  $T = 1.8$  K ( $<T_C$ ). (f) A zoomed-in view of panel (e) below 1 T.

to the change of Fermi surface shown in Fig. 3.  $R_0$  is positive and increases slowly between  $x = 0$  and 0.5, then increases rapidly until  $x = 0.85$ , and finally becomes negative abruptly at  $x = 1$ . Both the different  $|R_0|/|R_S|$  ratios and different behaviors of the two Hall coefficients at  $x \leq 0.5$  and  $x > 0.5$  suggest a transition from one regime to another at  $x = 0.5$ . Furthermore, we are plotting RRR values for each composition in Fig. 6(a), revealing two different regimes. For  $x \leq 0.5$ , RRR increases linearly as  $x$  increases, but it saturates to approximately 4 for  $x > 0.5$ . These observations motivate our second analysis.

We follow the empirical analysis, which was first proposed by Tian *et al.*<sup>17</sup> on iron thin films and was later justified theoretically.<sup>31,32</sup> The analysis assumes a material not in the clean limit where the residual resistivity  $\rho_{xx0}$  plays an important role, while the phonon scattering does not. These conditions are satisfied in PrAlGe $_{1-x}$ Si $_x$  where  $RRR \leq 4$  and the AHE occurs below 17 K, so phonon

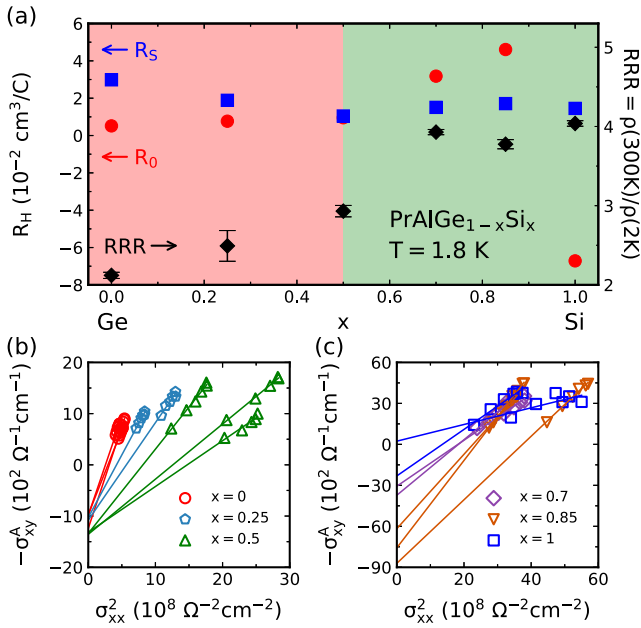


**FIG. 6.** (a) Ordinary Hall coefficient ( $R_0$ ), anomalous Hall coefficient ( $R_S$ ), and residual resistivity ratio (RRR) are plotted as red circles, blue squares, and black diamonds, respectively, as a function of  $x$  in  $\text{PrAlGe}_{1-x}\text{Si}_x$  at  $T = 1.8$  K. The errorbars for  $R_0$  and  $R_S$  are within the marker size, and the errorbar for RRR represents the range of RRR values for each composition. The red ( $x \leq 0.5$ ) and green ( $x > 0.5$ ) backgrounds distinguish two regions where the scaling analysis yields (b) the same intercept or (c) different intercepts according to Eq. (3).

scattering is negligible. Under such circumstance, the AHE can be described as

$$\rho_{xy}^A = (\alpha\rho_{xx0} + \beta\rho_{xx0}^2) + b\rho_{xx}^2, \quad (2)$$

where the coefficients  $\alpha$ ,  $\beta$ , and  $b$  parameterize the skew-scattering, side-jump, and intrinsic contributions to  $\rho_{xy}^A$ , respectively. The first two parameters depend on the impurity scattering in a specific sample, but the parameter  $b$  is independent of scattering. In general, the side-jump mechanism could also contribute to  $b$  through the same  $\rho_{xx}^2$  dependence.<sup>32,33</sup> However, in a material with topological band structures, we expect the intrinsic contribution to be dominant. Dividing both sides of Eq. (2) by  $\rho_{xx}^2$  (and assuming that  $\rho_{xx} \gg \rho_{xy}^A$ )<sup>34</sup> yields

$$\sigma_{xy}^A = -(\alpha\sigma_{xx0}^{-1} + \beta\sigma_{xx0}^{-2})\sigma_{xx}^2 - b, \quad (3)$$

where  $\sigma_{xx0} = 1/\rho_{xx0}$  is the residual conductivity and  $\sigma_{xy}^A = -\rho_{xy}^A/\rho_{xx}^2$  is the anomalous Hall conductivity (AHC). The first term in Eq. (3) depends on the residual conductivity and is sample dependent. However, the second term ( $b$ ) is sample independent and constitutes the intrinsic contribution to the AHC.

Following Eq. (3), we measured two to three samples for each composition of  $\text{PrAlGe}_{1-x}\text{Si}_x$  and determined  $b$  from the intercept of a linear fit to  $\sigma_{xy}^A$  as a function of  $\sigma_{xx}^2$ . For example, the

three datasets with green triangles in Fig. 6(b) correspond to three samples of  $\text{PrAlGe}_{0.5}\text{Si}_{0.5}$ . Their respective linear fits have different slopes showing different disorder levels, thus different  $\alpha$  and  $\beta$  fitting parameters in Eq. (3). However, all three lines end at the same intercept ( $b$ ) in the limit of  $\sigma_{xx} \rightarrow 0$ . The convergence of all linear fits strongly suggests an intrinsic mechanism for the AHE, which does not depend on the details of disorder level and only cares about the overall band structure. Interestingly,  $b$  seems to be the same in the three compositions  $x = 0, 0.25$ , and  $0.5$ , which is reasonably justified by the similar nodal structure of all  $\text{PrAlGe}_{1-x}\text{Si}_x$ , as illustrated in Figs. 3(c) and 3(f). The magnitude of  $\sigma_{xy}^{int} = -b \approx 10^3 \Omega^{-1} \text{cm}^{-1}$  is also consistent with the magnitude of the resonant AHE caused by the intrinsic mechanism.<sup>35,36</sup> Therefore, Fig. 6(b) suggests a universal intrinsic AHE in samples with  $x \leq 0.5$ . In contrast to Fig. 6(b), Fig. 6(c) shows that the parameter  $b$  varies randomly among samples with  $x > 0.5$ , hence the absence of a universal  $\sigma_{xy}^{int}$ . The failure of the scaling analysis suggests a predominantly extrinsic contribution to the AHC. Thus, we conclude that the AHE evolves from an intrinsic regime ( $x \leq 0.5$ ) to an extrinsic one ( $x > 0.5$ ) in  $\text{PrAlGe}_{1-x}\text{Si}_x$ , despite similar Weyl node structures in both end members,  $\text{PrAlGe}$  and  $\text{PrAlSi}$ .

## F. Discussion

Here, we discuss the possible reasons underlying the transition from the intrinsic to extrinsic AHE in the  $\text{PrAlGe}_{1-x}\text{Si}_x$  family. First, we emphasize that the failure of the scaling analysis for  $x > 0.5$  does not imply that the intrinsic mechanism is absent, but only that the AHE is dominated by the extrinsic contribution in this regime. Earlier studies of itinerant ferromagnets show that the crossover from an intrinsic to extrinsic regime takes place as one approaches the clean limit.<sup>35,36</sup> This trend is consistent with the results of Figs. 4 and 6(a), which show that  $\sigma_{xx}$  and RRR increase with  $x$  until  $x = 0.7$  before it saturates. Larger values of both  $\sigma_{xx}$  and RRR with increasing  $x$  suggest that the system is approaching a cleaner limit where the extrinsic mechanisms become dominant as  $x$  increases.<sup>35</sup> Another factor that plays a role in the AHE for  $x > 0.5$  is the position of  $E_F$  relative to the spin-orbit coupled bands. Figures 3(a) and 3(b) show that along the  $\Gamma - X$  path,  $E_F$  crosses the conduction band in  $\text{PrAlGe}$ , but in  $\text{PrAlSi}$ ,  $E_F$  barely comes in contact with the conduction band and lies in a narrow gap. Notably, the occupied and unoccupied bands gapped out by spin-orbit coupling can possess finite Berry curvatures and opposite contributions to  $\sigma_{xy}^{int}$ .<sup>37,38</sup> When  $E_F$  lies away from the gap, as is the case in  $\text{PrAlGe}$ , only the electronic levels with small Berry curvatures will be populated with increasing

**TABLE I.** EDX results for various  $\text{PrAlGe}_{1-x}\text{Si}_x$  samples. The atomic weights derived from EDX spectra are normalized to Pr content. These results are subject to an error of  $\pm 0.05$ .

$y$	Pr	Al	Ge	Si	Si/(Si + Ge) ( $x$ )
0	1.00	1.00	0.00	1.07	1.00
0.5	1.00	0.90	0.47	0.49	0.51
0.75	1.00	1.08	0.37	0.82	0.69
0.9	1.00	0.95	0.15	0.87	0.85
1	1.00	0.82	0.00	0.86	1.00

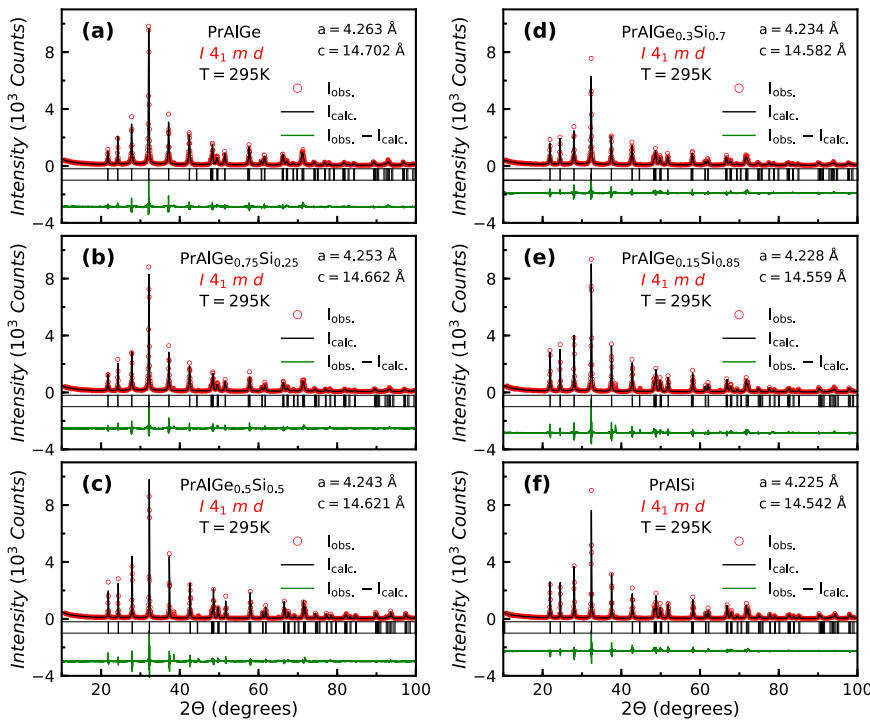


FIG. 7. Results of Rietveld refinement of powder x-ray diffraction data for different compositions.

temperature so that  $\sigma_{xy}^{int}$  will not change substantially. In contrast, when  $E_F$  lies in the gap between the occupied and unoccupied bands (PrAlSi case), with increasing temperature, the unoccupied band will start to be populated and significantly reduce  $\sigma_{xy}^{int}$ .  $\sigma_{xy}^{int}$  will, then, acquire a temperature dependence that leads to the failure of the scaling analysis. The proximity to the clean limit and the relative position of  $E_F$  to the spin-orbit coupled bands together may explain why the scaling fails for  $x > 0.5$  and the transition from intrinsic to extrinsic AHE in  $\text{PrAlGe}_{1-x}\text{Si}_x$ .

ACKNOWLEDGMENTS

We would like to thank Chunli Huang and Hiroaki Ishizuka for helpful discussions. The work at Boston College was funded by the National Science Foundation through Grant No. NSF/DMR-1708929. The work at Northeastern University was supported by the U.S. Department of Energy (DOE), Office of Basic Energy Sciences, Grant No. DE-FG02-07ER46352, and benefited by Northeastern University’s Advanced Scientific Computation Center and the National Energy Research Scientific Computing Center through DOE Grant No. DE-AC02-05CH11231. The National High Magnetic Field Laboratory is supported by the National Science Foundation through Grant No. NSF/DMR-1644779 and the State of Florida.

APPENDIX A: EDX RESULTS

We performed an EDX analysis to accurately evaluate the Si-content ( $x$ ) in  $\text{PrAlGe}_{1-x}\text{Si}_x$ . The first column in Table I shows

the mole ratio used in the crystal growth process (Pr:Al:Ge:Si = 1:10:y:1 - y). The last column gives the final Si-content ( $x$ ) in various  $\text{PrAlGe}_{1-x}\text{Si}_x$  crystals. For  $y = 0, 0.5$  and  $1, x = y$ . For  $y = 0.75$  and  $0.9, x = 0.7$  and  $0.85$ , respectively.

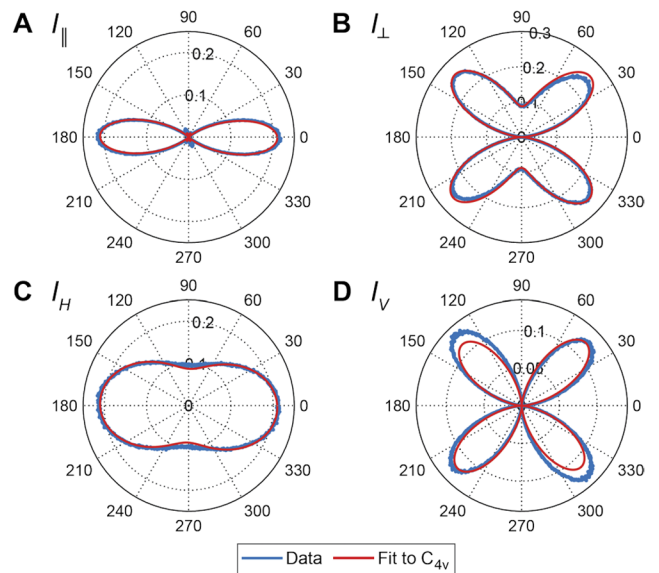


FIG. 8. The SHG data for incoming wavelength of 1500 nm, outgoing wavelength of 750 nm, and the corresponding fits to the bulk electric dipolar SHG in the  $C_{4v}$  point group as given by Eqs. (C1)–(C4) for (a)  $I_{\parallel}$ , (b)  $I_{\perp}$ , (c)  $I_V$ , and (d)  $I_H$ .

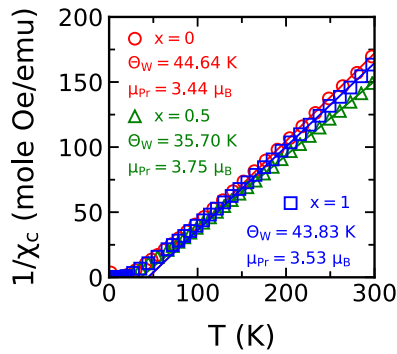


FIG. 9. Curie-Weiss analysis for  $\text{PrAlGe}_{1-x}\text{Si}_x$  for  $x = 0, 0.5$ , and  $1$ .

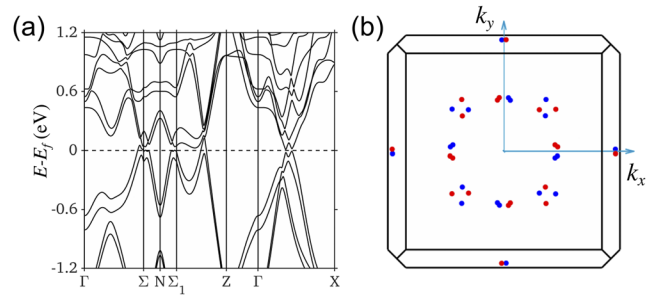


FIG. 10. (a) Band structure and (b) distribution of Weyl nodes in the momentum space in  $\text{PrAlGe}_{1-x}\text{Si}_x$  for  $x = 0.5$ . We get 40 Weyl nodes in the Brillouin zone similar to the end members,  $\text{PrAlGe}$  and  $\text{PrAlSi}$ .

APPENDIX B: RIETVELD REFINEMENT

To extract the lattice parameters for various compositions, we performed Rietveld x-ray refinement for all cases and the results are shown in Fig. 7. The calculated x-ray diffraction patterns match well with the corresponding experimental patterns. Figure 1 shows that the extracted lattice parameters evolve continuously across the  $\text{PrAlGe}_{1-x}\text{Si}_x$  family.

APPENDIX C: SECOND HARMONIC GENERATION

The SHG data were fit to appropriate functions for four different experimental configurations: incoming polarization rotating, output polarizer fixed with polarization parallel to the crystalline  $[010]$  axis, denoted by  $I_H(\phi)$ ; incoming polarization rotating, output polarizer fixed with polarization parallel to the  $[10\bar{1}]$  axis, denoted by  $I_V(\phi)$ ; incoming polarization rotating, outgoing polarizer rotated

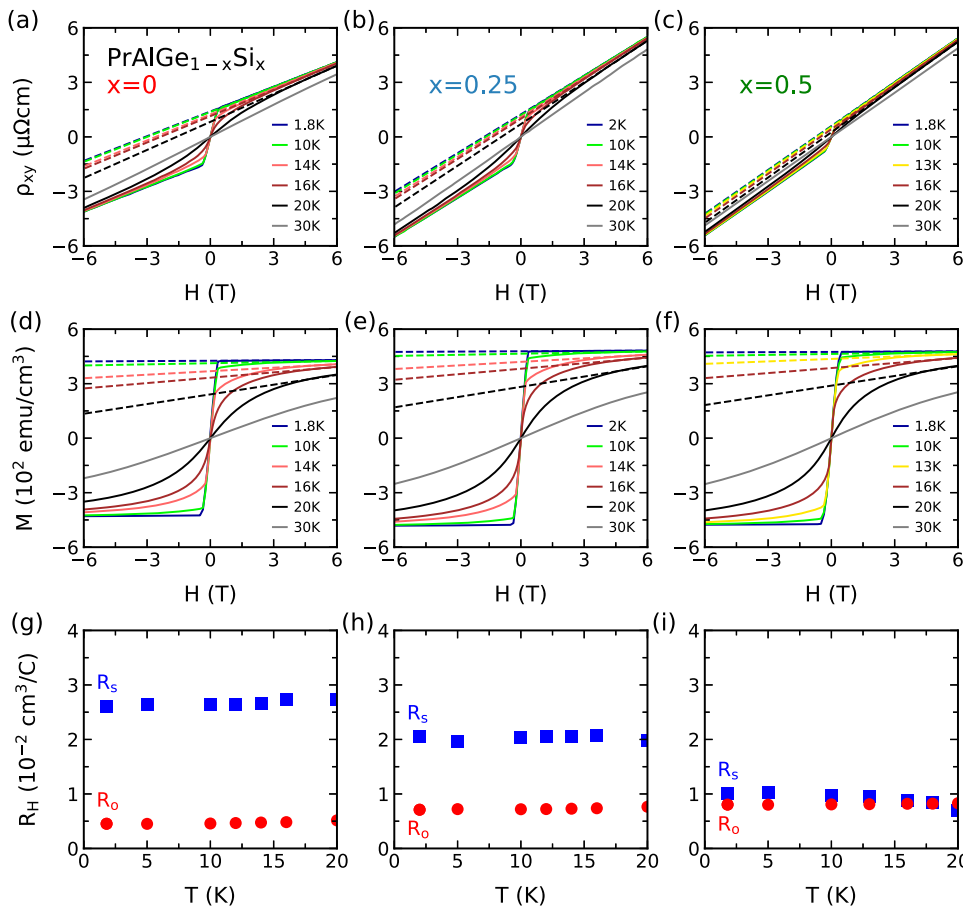


FIG. 11. Data used to extract  $R_0$  and  $R_S$  in  $\text{PrAlGe}_{1-x}\text{Si}_x$  compounds for  $x \leq 0.5$ . [(a)–(c)]  $\rho_{xy}$  measured at different temperatures. The y-intercepts of the fitting lines are extracted as  $\rho_{xy}^A$ . [(d)–(f)] Magnetization measured at different temperatures. Fitting lines are based on the high-field part of the data. [(g)–(i)]  $R_0$  and  $R_S$  values at different temperatures.

at  $0^\circ$  angle relative to the incoming polarization, denoted by  $I_{\parallel}(\phi)$ ; and incoming polarization rotating, outgoing polarizer rotated with the polarization axis at  $90^\circ$  angle relative to the incoming polarization, denoted by  $I_{\perp}(\phi)$ . In the electric dipole approximation, the mathematical forms of the various responses for the [101] crystal face in the  $I4_1md$  space group ( $C_{4v}$  point group) are given by

$$I_{\parallel}^{eee}(\phi) = \frac{1}{32} \cos^2(\phi) [(-2\chi_{xxz}^{eee} - \chi_{zxx}^{eee} + \chi_{zzz}^{eee}) \cos(2\phi) + 6\chi_{xxz}^{eee} + 3\chi_{zxx}^{eee} + \chi_{zzz}^{eee}]^2, \quad (C1)$$

$$I_{\perp}^{eee}(\phi) = \frac{1}{8} \sin^2(\phi) [(-2\chi_{xxz}^{eee} + \chi_{zxx}^{eee} + \chi_{zzz}^{eee}) \cos^2(\phi) + 2\chi_{zxx}^{eee} \sin^2(\phi)]^2, \quad (C2)$$

$$I_H^{eee}(\phi) = \frac{1}{8} [(2\chi_{xxz}^{eee} + \chi_{zxx}^{eee} + \chi_{zzz}^{eee}) \cos^2(\phi) + 2\chi_{zxx}^{eee} \sin^2(\phi)]^2, \quad (C3)$$

$$I_V^{eee}(\phi) = 2[\chi_{xxz}^{eee} \sin(\phi) \cos(\phi)]^2. \quad (C4)$$

The data were fit to expressions [(C1)–(C4)] accounting for a rotation of the sample axes relative to the laboratory x-axis to produce excellent fits to the data, as shown in Fig. 8. The competing space group assignment  $I4_1/amd$  (point group  $D_{4h}$ ) is centrosymmetric and, thus, should not produce as strong of a SHG response as we have shown here.

#### APPENDIX D: CURIE-WEISS ANALYSIS

Curie–Weiss analysis was performed on  $\text{PrAlGe}_{1-x}\text{Si}_x$  for  $x = 0, 0.5, \text{ and } 1$ . The Curie–Weiss fit was made to the high-temperature data ( $T > 150 \text{ K}$ ) to extract the Weiss temperature  $\Theta_W$  and the effective moment  $\mu_{\text{Pr}}$  (Fig. 9). Based on this analysis, different compositions of the  $\text{PrAlGe}_{1-x}\text{Si}_x$  family are found to have similar values of  $\Theta_W$  and  $\mu_{\text{Pr}}$ .

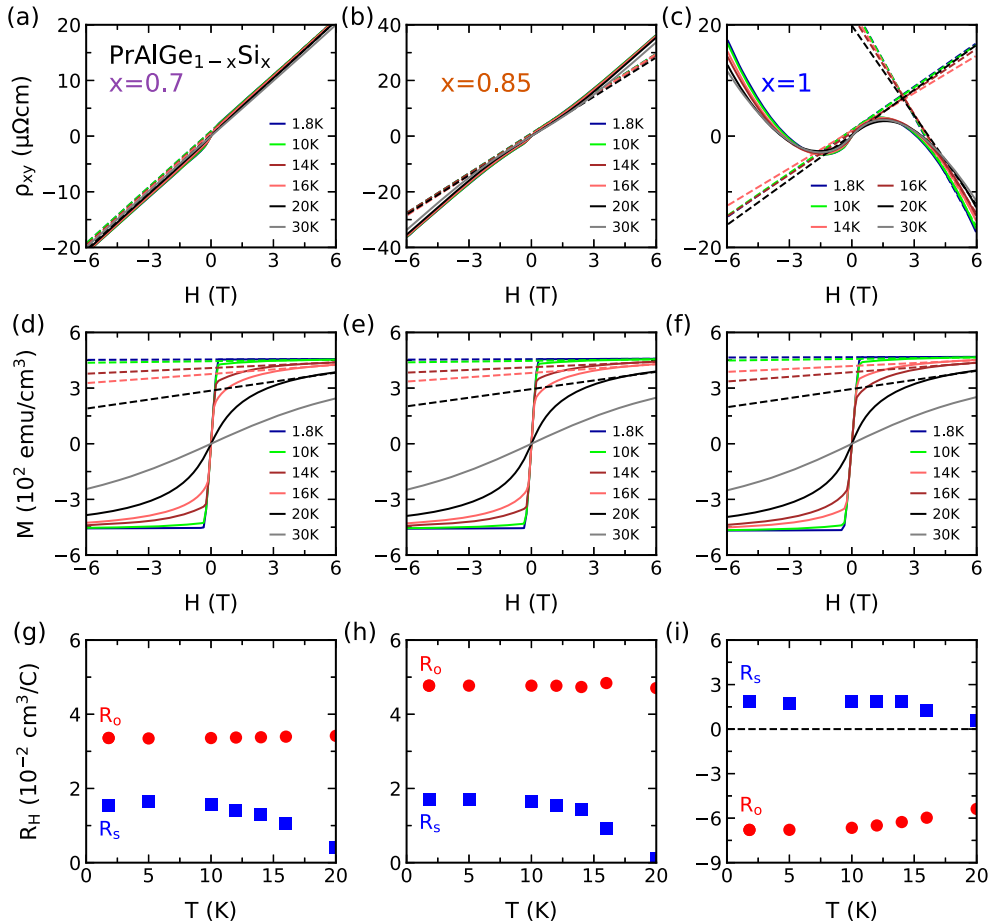


**FIG. 12.** Data used to extract  $R_0$  and  $R_S$  in  $\text{PrAlGe}_{1-x}\text{Si}_x$  compounds for  $x > 0.5$ . [(a)–(c)]  $\rho_{xy}$  measured at different temperatures. The y-intercepts of the fitting lines are extracted as  $\rho_{xy}^A$ . [(d)–(f)] Magnetization measured at different temperatures. Fitting lines are based on the high-field part of the data. [(g)–(i)]  $R_0$  and  $R_S$  values at different temperatures.

## APPENDIX E: TOPOLOGICAL ELECTRONIC STRUCTURE OF $\text{PrAlGe}_{1-x}\text{Si}_x$ FOR $x = 0.5$

The calculated band structure of  $\text{PrAlGe}_{1-x}\text{Si}_x$  for  $x = 0.5$  in the presence of SOC is shown in Fig. 10(a). It has both electron and hole band crossings at the Fermi level, which are similar to those in the end members  $\text{PrAlGe}$  and  $\text{PrAlSi}$ . There are 40 Weyl nodes whose Brillouin zone distribution remains similar to that of  $\text{PrAl}(\text{Ge},\text{Si})$  [see Fig. 10(b)]. These results, further, show that the Weyl state remains robust with changes in Si concentration.

## APPENDIX F: THE ANALYSIS OF $R_0$ AND $R_S$

Here, we show all the data needed to extract  $R_0$  and  $R_S$  values according to Eq. (1) in Figs. 11 and 12. Note that, for  $x = 0.85$  and  $x = 1$ ,  $\rho_{xy}$  is not linear at high fields. Thus, to extract  $\rho_{xy}^A$  for these two compositions, the data between  $H = 0.5$  T and 1 T were fitted to a straight line, the intercept of which at  $H = 0$  T was extracted as  $\rho_{xy}^A$ . For other compositions, the data at  $H > 4$  T were used for the fitting lines to extract  $\rho_{xy}^A$ . Slopes of these lines are reported as  $R_0$  except for  $x = 1$ , where a second fitting line was made to the high-field data to capture the behavior of the ordinary Hall effect.

## APPENDIX G: QUANTUM OSCILLATION AND CALCULATED ANOMALOUS HALL CONDUCTIVITY

Results of quantum oscillation (QO) experiments and the calculated AHCs are given in Fig. 13. Note that to match the

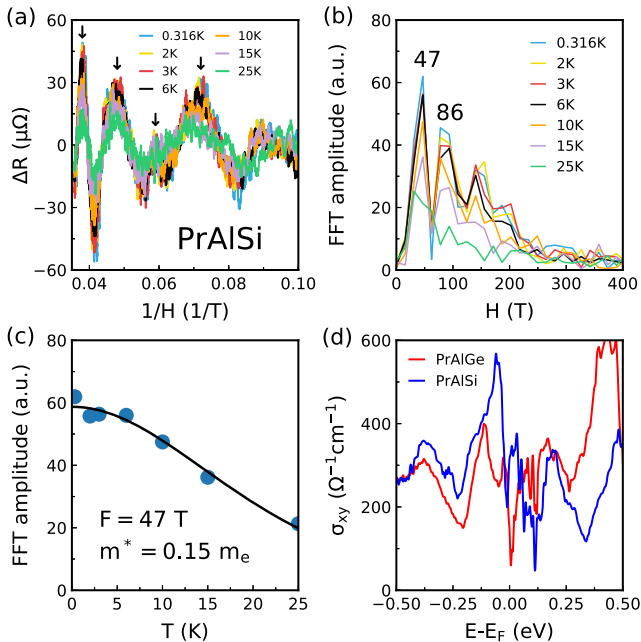


**FIG. 13.** (a) Shubnikov-de Haas oscillations in  $\text{PrAlSi}$ . The field was applied along the  $c$ -axis. The arrows mark the peaks of the oscillations. (b) Fast Fourier transform (FFT) of the data shown in (a). (c) Effective mass extracted by the Lifshitz-Kosevich formula<sup>39</sup> for the Fermi surface corresponds to  $F = 47$  T. (d) Calculated intrinsic AHC for  $\text{PrAlGe}$  and  $\text{PrAlSi}$ .

experimental and theoretical frequencies, the  $E_F$  in the calculations should be at 6 meV for  $\text{PrAlSi}$ . At 6 meV in Fig. 13(d), the calculated AHC is about  $300\text{--}400 \Omega^{-1} \text{cm}^{-1}$  for  $\text{PrAlSi}$ . Since the calculation here only considers the contribution from the Berry curvature, there could be a discrepancy as shown in the literature.<sup>33</sup> Overall, the magnitude of the calculated AHC is comparable to the experimental one.

## APPENDIX H: ENERGIES AND POSITIONS OF THE WEYL NODES IN $\text{PrAlGe}$ AND $\text{PrAlSi}$

We have examined the band structures to search for Weyl nodes, which are sources and drains of the Berry curvature. In both

**TABLE II.** Energies and positions of Weyl nodes in  $\text{PrAlGe}$ .

WP	$k_x$ ( $\text{\AA}^{-1}$ )	$k_y$ ( $\text{\AA}^{-1}$ )	$k_z$ ( $\text{\AA}^{-1}$ )	$E - E_F$ (eV)	Charge
1	0.342 98	0.288 01	0.001 26	-0.036	-1
2	-0.288 01	0.342 98	0.001 26	-0.036	-1
3	0.288 01	-0.342 98	0.001 26	-0.036	-1
4	-0.342 98	-0.288 01	0.001 26	-0.036	-1
5	0.041 10	-0.346 97	0.281 12	0.027	-1
6	0.346 97	0.041 10	0.281 12	0.027	-1
7	-0.346 97	-0.041 10	0.281 12	0.027	-1
8	-0.041 10	+0.346 97	0.281 12	0.027	-1
9	-0.244 97	-0.270 41	-0.000 56	-0.031	-1
10	0.270 41	-0.244 97	-0.000 56	-0.031	-1
11	-0.270 41	0.244 97	-0.000 56	-0.031	-1
12	0.244 97	0.270 41	-0.000 56	-0.031	-1
13	0.771 59	0.012 09	-0.012 92	0.05	+1
14	-0.012 09	0.771 59	-0.012 92	0.05	+1
15	0.012 09	-0.771 59	-0.012 92	0.05	+1
16	-0.771 59	-0.012 09	-0.012 92	0.05	+1
17	-0.028 71	0.367 69	-0.293 16	0.67	-1
18	-0.367 69	-0.028 71	-0.293 16	0.67	-1
19	0.367 69	0.028 71	-0.293 16	0.67	-1
20	0.028 71	-0.367 69	-0.293 16	0.67	-1
21	-0.342 42	0.288 18	-0.001 35	-0.034	+1
22	-0.288 18	-0.342 42	-0.001 35	-0.034	+1
23	0.288 18	0.342 42	-0.001 35	-0.034	+1
24	0.342 42	-0.288 18	-0.001 35	-0.034	+1
25	-0.027 71	-0.363 09	0.297 22	0.071	+1
26	0.363 09	-0.027 71	0.297 22	0.071	+1
27	-0.363 09	0.027 71	0.297 22	0.071	+1
28	0.027 71	0.363 09	0.297 22	0.071	+1
29	0.246 54	-0.270 31	0.015 89	-0.032	+1
30	0.270 31	0.246 54	0.015 89	-0.032	+1
31	-0.270 31	-0.246 54	0.015 89	-0.032	+1
32	-0.246 54	0.270 31	0.015 89	-0.032	+1
33	-0.773 07	0.012 65	0.014 09	0.046	-1
34	-0.012 65	-0.773 07	0.014 09	0.046	-1
35	0.012 65	0.773 07	0.014 09	0.046	-1
36	0.773 07	-0.012 65	0.014 09	0.046	-1
37	0.040 59	0.346 01	-0.284 72	0.028	+1
38	0.346 01	0.040 59	-0.284 72	0.028	+1
39	0.346 01	0.040 59	-0.284 72	0.028	+1
40	0.040 59	0.346 01	-0.284 72	0.028	+1

TABLE III. Energies and positions of Weyl nodes in PrAlSi.

WP	$k_x$ ( $\text{\AA}^{-1}$ )	$k_y$ ( $\text{\AA}^{-1}$ )	$k_z$ ( $\text{\AA}^{-1}$ )	$E - E_F$ (eV)	Charge
1	0.376 95	0.294 62	-0.000 16	0.017	-1
2	-0.294 62	0.376 95	-0.000 16	0.017	-1
3	0.294 62	-0.376 95	-0.000 16	0.017	-1
4	-0.376 95	-0.294 62	-0.000 16	0.017	-1
5	0.047 1	-0.353 4	0.256 0	-0.002	-1
6	0.353 4	0.047 1	0.256 0	-0.002	-1
7	-0.353 4	-0.047 1	0.256 0	-0.002	-1
8	-0.047 1	0.353 4	0.256 0	-0.002	-1
9	-0.247 4	-0.304 6	0.013 5	0.006	-1
10	0.304 6	-0.247 4	0.013 5	0.006	-1
11	-0.304 6	0.247 4	0.013 5	0.006	-1
12	0.247 4	0.304 6	0.013 5	0.006	-1
13	0.763 71	0.015 71	-0.016 10	0.07	+1
14	-0.015 71	0.763 71	-0.016 10	0.07	+1
15	0.015 71	-0.763 71	-0.016 10	0.07	+1
16	-0.763 71	-0.015 71	-0.016 10	0.07	+1
17	-0.030 81	0.381 76	-0.257 08	0.046	-1
18	-0.381 76	-0.030 81	-0.257 08	0.046	-1
19	0.381 76	0.030 81	-0.257 08	0.046	-1
20	0.030 81	-0.381 76	-0.257 08	0.046	-1
21	-0.376 18	0.295 00	0.000 03	0.018	+1
22	-0.295 00	-0.376 18	0.000 03	0.018	+1
23	0.295 00	0.376 18	0.000 03	0.018	+1
24	0.376 18	-0.295 00	0.000 03	0.018	+1
25	-0.030 95	-0.380 96	0.256 78	0.047	+1
26	0.380 96	-0.030 95	0.256 78	0.047	+1
27	-0.380 96	0.030 95	0.256 78	0.047	+1
28	0.030 95	0.380 96	0.256 78	0.047	+1
29	0.248 50	-0.304 26	0.018 82	0.004	+1
30	0.304 26	0.248 50	0.018 82	0.004	+1
31	-0.304 26	-0.248 50	0.018 82	0.004	+1
32	-0.248 50	+0.304 26	0.018 82	0.004	+1
33	-0.763 89	0.015 73	0.016 58	0.07	-1
34	-0.015 73	-0.763 89	0.016 58	0.07	-1
35	0.015 73	0.763 89	0.016 58	0.07	-1
36	0.763 89	-0.015 73	0.016 58	0.07	-1
37	0.047 01	0.353 06	-0.255 80	-0.002	+1
38	-0.353 06	0.047 01	-0.255 80	-0.002	+1
39	0.353 06	-0.047 01	-0.255 80	-0.002	+1
40	-0.047 01	-0.353 06	-0.255 80	-0.002	+1

PrAlGe and PrAlSi, we identified 40 Weyl nodes; their positions in  $k$ -space and energies with respect to  $E_F$  are listed in Tables II and III.

## REFERENCES

- E. M. Pugh and N. Rostoker, "Hall effect in ferromagnetic materials," *Rev. Mod. Phys.* **25**, 151–157 (1953).
- N. Nagaosa, J. Sinova, S. Onoda, A. H. MacDonald, and N. P. Ong, "Anomalous Hall effect," *Rev. Mod. Phys.* **82**, 1539–1592 (2010).
- J. Smit, "The spontaneous Hall effect in ferromagnetics II," *Physica* **24**, 39–51 (1958).
- L. Berger, "Side-jump mechanism for the Hall effect of ferromagnets," *Phys. Rev. B* **2**, 4559–4566 (1970).
- R. Karplus and J. M. Luttinger, "Hall effect in ferromagnetics," *Phys. Rev.* **95**, 1154–1160 (1954).
- G. Sundaram and Q. Niu, "Wave-packet dynamics in slowly perturbed crystals: Gradient corrections and Berry-phase effects," *Phys. Rev. B* **59**, 14915–14925 (1999).
- T. Jungwirth, Q. Niu, and A. H. MacDonald, "Anomalous Hall effect in ferromagnetic semiconductors," *Phys. Rev. Lett.* **88**, 207208 (2002).
- Y. Yao, L. Kleinman, A. H. MacDonald, J. Sinova, T. Jungwirth, D.-s. Wang, E. Wang, and Q. Niu, "First principles calculation of anomalous Hall conductivity in ferromagnetic bcc Fe," *Phys. Rev. Lett.* **92**, 037204 (2004).
- A. Burkov, "Anomalous Hall effect in Weyl metals," *Phys. Rev. Lett.* **113**, 187202 (2014).
- W. Witczak-Krempa, G. Chen, Y. B. Kim, and L. Balents, "Correlated quantum phenomena in the strong spin-orbit regime," *Annu. Rev. Condens. Matter Phys.* **5**, 57–82 (2014).
- K. Ueda, R. Kaneko, H. Ishizuka, J. Fujioka, N. Nagaosa, and Y. Tokura, "Spontaneous Hall effect in the Weyl semimetal candidate of all-in-all-out pyrochlore iridate," *Nat. Commun.* **9**, 3032 (2018).
- I. Belopolski, K. Manna, D. S. Sanchez, G. Chang, B. Ernst, J. Yin, S. S. Zhang, T. Cochran, N. Shumiya, H. Zheng, B. Singh, G. Bian, D. Multer, M. Litskevich, X. Zhou, S.-M. Huang, B. Wang, T.-R. Chang, S.-Y. Xu, A. Bansil, C. Felser, H. Lin, and M. Z. Hasan, "Discovery of topological Weyl fermion lines and drumhead surface states in a room temperature magnet," *Science* **365**, 1278–1281 (2019).
- K. Manna, Y. Sun, L. Muechler, J. Kübler, and C. Felser, "Heusler, Weyl and Berry," *Nat. Rev. Mater.* **3**, 244–256 (2018).
- T. Suzuki, R. Chisnell, A. Devarakonda, Y.-T. Liu, W. Feng, D. Xiao, J. W. Lynn, and J. Checkelsky, "Large anomalous Hall effect in a half-Heusler antiferromagnet," *Nat. Phys.* **12**, 1119 (2016).
- E. Liu, Y. Sun, N. Kumar, L. Muechler, A. Sun, L. Jiao, S.-Y. Yang, D. Liu, A. Liang, Q. Xu, J. Kroder, V. Süß, H. Borrmann, C. Shekhar, Z. Wang, C. Xi, W. Wang, W. Schnelle, S. Wirth, Y. Chen, S. T. B. Goennenwein, and C. Felser, "Giant anomalous Hall effect in a ferromagnetic kagome-lattice semimetal," *Nat. Phys.* **14**, 1125–1131 (2018).
- L. Ye, M. Kang, J. Liu, F. Von Cube, C. R. Wicker, T. Suzuki, C. Jozwiak, A. Bostwick, E. Rotenberg, D. C. Bell *et al.*, "Massive Dirac fermions in a ferromagnetic kagome metal," *Nature* **555**, 638 (2018).
- Y. Tian, L. Ye, and X. Jin, "Proper scaling of the anomalous Hall effect," *Phys. Rev. Lett.* **103**, 087206 (2009).
- B. Meng, H. Wu, Y. Qiu, C. Wang, Y. Liu, Z. Xia, S. Yuan, H. Chang, and Z. Tian, "Large anomalous Hall effect in ferromagnetic Weyl semimetal candidate PrAlGe," *APL Mater.* **7**, 051110 (2019).
- P. Pupal, C. Mielke, N. Kumar, Y. Soh, T. Shang, M. Medarde, J. S. White, and E. Pomjakushina, "Bulk single-crystal growth of the theoretically predicted magnetic Weyl semimetals RAlGe (R = Pr, Ce)," *Phys. Rev. Mater.* **3**, 024204 (2019).
- G. Kresse and J. Furthmüller, "Efficient iterative schemes for *ab initio* total-energy calculations using a plane-wave basis set," *Phys. Rev. B* **54**, 11169–11186 (1996).
- G. Kresse and D. Joubert, "From ultrasoft pseudopotentials to the projector augmented-wave method," *Phys. Rev. B* **59**, 1758–1775 (1999).
- J. P. Perdew, K. Burke, and M. Ernzerhof, "Generalized gradient approximation made simple," *Phys. Rev. Lett.* **77**, 3865–3868 (1996).
- N. Marzari and D. Vanderbilt, "Maximally localized generalized Wannier functions for composite energy bands," *Phys. Rev. B* **56**, 12847–12865 (1997).
- G. Chang, B. Singh, S.-Y. Xu, G. Bian, S.-M. Huang, C.-H. Hsu, I. Belopolski, N. Alidoust, D. S. Sanchez, H. Zheng, H. Lu, X. Zhang, Y. Bian, T.-R. Chang, H.-T. Jeng, A. Bansil, H. Hsu, S. Jia, T. Neupert, H. Lin, and M. Z. Hasan, "Magnetic and noncentrosymmetric Weyl fermion semimetals in the RAlGe family of compounds (R = rare-earth)," *Phys. Rev. B* **97**, 041104 (2018).
- B. Lv, H. Weng, B. Fu, X. Wang, H. Miao, J. Ma, P. Richard, X. Huang, L. Zhao, G. Chen, Z. Fang, X. Dai, T. Qian, and H. Ding, "Experimental discovery of Weyl semimetal TaAs," *Phys. Rev. X* **5**, 031013 (2015).

- <sup>26</sup>L. X. Yang, Z. K. Liu, Y. Sun, H. Peng, H. F. Yang, T. Zhang, B. Zhou, Y. Zhang, Y. F. Guo, M. Rahn, D. Prabhakaran, Z. Hussain, S.-K. Mo, C. Felser, B. Yan, and Y. L. Chen, "Weyl semimetal phase in the non-centrosymmetric compound TaAs," *Nat. Phys.* **11**, 728–732 (2015).
- <sup>27</sup>S.-Y. Xu, N. Alidoust, G. Chang, H. Lu, B. Singh, I. Belopolski, D. S. Sanchez, X. Zhang, G. Bian, H. Zheng, M.-A. Husanu, Y. Bian, S.-M. Huang, C.-H. Hsu, T.-R. Chang, H.-T. Jeng, A. Bansil, T. Neupert, V. N. Strocov, H. Lin, S. Jia, and M. Z. Hasan, "Discovery of Lorentz-violating type II Weyl fermions in LaAlGe," *Sci. Adv.* **3**, e1603266 (2017).
- <sup>28</sup>H. Hodovanets, C. J. Eckberg, P. Y. Zavalij, H. Kim, W.-C. Lin, M. Zic, D. J. Campbell, J. S. Higgins, and J. Paglione, "Single-crystal investigation of the proposed type-II Weyl semimetal CeAlGe," *Phys. Rev. B* **98**, 245132 (2018).
- <sup>29</sup>T. Suzuki, L. Savary, J.-P. Liu, J. W. Lynn, L. Balents, and J. G. Checkelsky, "Singular angular magnetoresistance in a magnetic nodal semimetal," *Science* **365**, 377–381 (2019).
- <sup>30</sup>H.-Y. Yang, T. Nummy, H. Li, S. Jaszewski, M. Abramchuk, D. Dessau, and F. Tafti, "Extreme magnetoresistance in the topologically trivial lanthanum monopnictide LaAs," *Phys. Rev. B* **96**, 235128 (2017).
- <sup>31</sup>A. Shitade and N. Nagaosa, "Anomalous Hall effect in ferromagnetic metals: Role of phonons at finite temperature," *J. Phys. Soc. Jpn.* **81**, 083704 (2012).
- <sup>32</sup>D. Hou, G. Su, Y. Tian, X. Jin, S. A. Yang, and Q. Niu, "Multivariable scaling for the anomalous Hall effect," *Phys. Rev. Lett.* **114**, 217203 (2015).
- <sup>33</sup>J. Weischenberg, F. Freimuth, J. Sinova, S. Blügel, and Y. Mokrousov, "Ab initio theory of the scattering-independent anomalous Hall effect," *Phys. Rev. Lett.* **107**, 106601 (2011).
- <sup>34</sup>In the limit  $\rho_{xx} \gg \rho_{xy}^A$ , the relations  $\sigma_{xy}^A \sim \rho_{xy}^A/\rho_{xx}^2$  and  $\sigma_{xx} \sim 1/\rho_{xx}^2$  are valid. In PrAlGe<sub>1-x</sub>Si<sub>x</sub>, this is the case as shown in the resistivity data ( $\rho_{xy}^A$  in Fig. 5(f) and  $\rho_{xx}$  in Fig. 4).
- <sup>35</sup>S. Onoda, N. Sugimoto, and N. Nagaosa, "Intrinsic versus extrinsic anomalous Hall effect in ferromagnets," *Phys. Rev. Lett.* **97**, 126602 (2006).
- <sup>36</sup>T. Miyasato, N. Abe, T. Fujii, A. Asamitsu, S. Onoda, Y. Onose, N. Nagaosa, and Y. Tokura, "Crossover behavior of the anomalous Hall effect and anomalous Nernst effect in itinerant ferromagnets," *Phys. Rev. Lett.* **99**, 086602 (2007).
- <sup>37</sup>D. Xiao, M.-C. Chang, and Q. Niu, "Berry phase effects on electronic properties," *Rev. Mod. Phys.* **82**, 1959 (2010).
- <sup>38</sup>L. Ye, Y. Tian, X. Jin, and D. Xiao, "Temperature dependence of the intrinsic anomalous Hall effect in nickel," *Phys. Rev. B* **85**, 220403 (2012).
- <sup>39</sup>D. Shoenberg, *Magnetic Oscillations in Metals* (Cambridge University Press, 2009).